Available online at www.sciencedirect.com

ScienceDirect

International Journal of Solids and Structures 43 (2006) 7820–7839

INTERNATIONAL JOURNAL OF SOLIDS and STRUCTURES

www.elsevier.com/locate/ijsolstr

A phenomenological high strain rate model with failure for ice

Kelly S. Carney [a], David J. Benson [b,*], Paul DuBois [c], Ryan Lee [d]

[a] *NASA Glenn Research Center, 21000 Brookpark Road, Cleveland, OH 44135, USA*

[b] *Department of Mechanical and Aerospace Engineering, University of California, Mail Stop 0411, San Diego, 9500 Gilman Drive, La Jolla, CA 92093-0411, USA*

[c] *Freiligrathstrasse 6, 63071 Offenbach, Germany*

[d] *The Boeing Company, Rotorcraft Division, Structures, Technology, and Prototyping, Industrial Hwy and Stewert Ave., Ridley Park, PA 19078, USA*

Received 29 November 2005; received in revised form 15 March 2006
Available online 15 April 2006

Abstract

Modeling the high velocity impact of ice was a requirement in the safety calculations for the return-to-flight of the Space Shuttle on July 26, 2005. Ice, however, is not a common structural material and commercial finite element programs did not have any appropriate models. A phenomenological model with failure was developed to match experimental ballistic tests. The model has a relatively small number of material constants, most of which have been measured experimentally. A description of the model and comparisons of calculations to experiments are presented.

Keywords: Finite element; Eulerian; Impact; Ice; Plasticity

1. Introduction

The destructive effects of the impact of ice at high speeds is well known. For man-rated vehicles, experiments are usually required to certify the safety of the design. Jet engines, for example, are required to pass ice ingestion tests by the FAA. Concern about the impact of ice on the Space Shuttle dates back to at least the 1983 test program described by DeWolfe (1983).

Analyses were rarely carried out previously for many reasons, including the absence of sufficient computer power, software that could handle both the extreme deformations of the ice and accurately model the structural response of the vehicle, and an accurate model for ice. Low cost PC clusters have provided the required computer power. Finite element methods have advanced dramatically since DeWolfe's investigation. There

* Corresponding author. Tel.: +1 619 534 5928; fax: +1 858 534 7078.
E-mail address: dbenson@ucsd.edu (D.J. Benson).

0020-7683/$ - see front matter
doi:10.1016/j.ijsolstr.2006.04.005

has been, however, little effort previously in the development of a constitutive model for ice that can be used in finite element calculations.

The Columbia Space Shuttle tragedy motivated a large scale safety review of the Space Shuttle, and included in that review was a requirement for certifying the ability of the leading edge of the wing to safely sustain impacts of various types of debris (Columbia Accident Investigation Board, 2003). The leading edge is made of carbon–carbon composites, with each section costing over one million dollars. Given the wide range of debris, impact locations, and velocities, and the many months it takes to produce a single panel, a complete experimental test program would be prohibitively expensive and could not be accomplished in a timely manner. Finite element analyses, carefully validated by a series of experiments, was therefore required to certify the Space Shuttle for flight.

After calculating the relative velocity of the leading edge and debris, analyses were limited to low density materials that would rapidly decelerate in the atmosphere. Dense objects, such as bolts, are not believed to endanger the leading edge since the relative impact velocity would be low. Low density materials, such as the foam that brought down Columbia, rapidly decelerate to the point that the Shuttle flies into the debris at a velocity up to 3000 ft/s. Ice decelerates rapidly enough to be considered a potential problem, with a maximum expected impact velocity of up to 1000 ft/s.

Constitutive models for reinforced carbon–carbon composites and the low density foams covering the external fuel tank are reasonably mature, and validation experiments using the shuttle materials demonstrated their accuracy. Ice, however, is not a commercial structural material, and aside from high velocity impact situations of interest to the aerospace industry, is rarely subject to high strain rate impact conditions. Although ice has been studied extensively, e.g., Schulson (2001), only a very few efforts have been made to model it numerically at high strain rates (Kim and Kedward, 2000; Kim et al., 2003). Attempts to use existing models, including some intended for brittle engineering materials, demonstrated the need for an improved model.

The ice model presented here was developed under the deadlines required to return the Space Shuttle to flight. It is phenomenological in nature, and its value was judged based on how well it modeled the ballistic experiments. As far as possible, the material parameters have been measured by experiments that are independent of the experiments used to validate the accuracy of the ice model. No attempt has been made to include micromechanical or first principles models of the comminution of ice or its response after impact. More sophisticated models could and should be developed.

2. The engineering properties of ice

This section relies heavily on the review papers by Schulson (2001) and Petrovic (2003). Schulson provides 180 references, and Petrovic, 48, and therefore this section only briefly summarizes the properties of interest to the current work. Much of the literature on ice mechanics is associated with geophysical applications or arctic ship operations, and it is not discussed here. Our focus is on modeling ice that will do the most ballistic damage at a given velocity, i.e., the strongest, toughest ice. We will, therefore, omit discussions about the effects of salinity, inclusions, and other structural defects that reduce the strength of ice.

Ice should be regarded as a class of materials rather than a single, specific material with well defined properties. It has thirteen different crystal structures and two amorphous states. The ice of interest to us is ice Ih, which has a hexagonal crystal structure and forms at ambient pressures. In the literature (Schulson, 2001), ice Ih is referred to as ordinary or terrestrial ice but since it is the only form of interest here, it will simply be referred to as ice. Some sample compressive strengths at $-10\,^{\circ}\mathrm{C}$, from Schulson et al. (2005), are given in Table 1. The strength of the columnar-grained polycrystal samples was obtained by loading the ice in a

Table 1
Sample ice static compressive strengths

Batch	Structure	Compressive strength (MPa) $\pm$ 1 SD
1	Single crystal	14.8 ± 2.3
3	Columnar	7.2 ± 0.9
4	Columnar	6.5 ± 1.8
5	Columnar	9.0 ± 1.4

direction parallel to the long axis of the grains, i.e., along the columns. Note that all of them include a range. Significant variations in the mechanical properties of carefully manufactured ice have been observed from batch to batch. It has also been shown by Carter (1971) that the strength of single crystal ice is also sensitive to the crystal orientation.

The ice used in the experiments, and characterized for NASA by Schulson et al. (2005), was manufactured by Ice Culture,Inc. of Hensall, Ontario, Canada, because it was thought to be the best chance to keep variations to a minimum. It is also a relatively strong ice, which is a requirement for validating impact safety, and it is optically transparent and very near theoretical density.

Like many brittle materials, ice is stronger in compression than in tension. Unlike most brittle materials, it exhibits its brittle behavior up to the melting point at strain rates that are too low for inertial confinement to play a role. Schulson (2001) states that single and polycrystals exhibit this behavior and attributes it to the basic deformation processes and not grain boundary behavior. Quoting Schulson (2001): "At root are sluggish dislocation kinetics ...Ice Ih slips preferentially on basal {0001} planes and this is impeded by the unique requirement of protonic rearrangement."

Both Petrovic (2003) and Schulson (2001) report that the strength of ice is a function of grain size and that it exhibits the Hall–Petch effect. For a constant grain size, the tensile failure stress is not sensitive to the strain rate. Schulson divides the tensile failure stress, σ_t, as a function of grain size, into two regimes demarcated by a critical grain size d_c, which decreases with strain rate. Above the critical grain size,

$$\sigma_t = \sigma_0 + k_t/\sqrt{d} \quad d > d_c \tag{1}$$

and below it,

$$\sigma_t = K/\sqrt{d} \quad d < d_c \tag{2}$$

where $\sigma_0 = 0.6$ MPa, $k_t = 0.02$ MPa$\sqrt{\text{m}}$, and $K = 0.044$ MPa$\sqrt{\text{m}}$ at -10 °C.

Schulson (2001) notes that ceramics exhibit similar improvements in their tensile failure stress, but that the ranges are reversed (i.e., Eq. (1) applies for $d < d_c$ for ceramics). He attributes the difference to the different mechanisms coming into play for the different materials. Ceramics contain pre-existing flaws and residual stresses while ice can be made free of internal flaws and stresses. The ice used in the experiments described in our work falls into this class of "perfect" ice and many of the specimens were also single crystals.

Failure in ice that does not initially contain flaws requires a nucleation mechanism in addition to crack propagation. Schulson (2001) believes that grain boundary sliding is the dominant nucleation mechanism, as opposed to dislocation pileups. Crack nucleation limits the tensile strength of ice with a grain size greater than d_c since once the crack nucleates in this regime, the stress is also high enough to propagate it.

Ice can exhibit a variety of behaviors, ranging from ductile to brittle, as a function of strain rate in compression (see Fig. 1). As in tensile failure, the compressive failure stress is dependent on the grain size. The

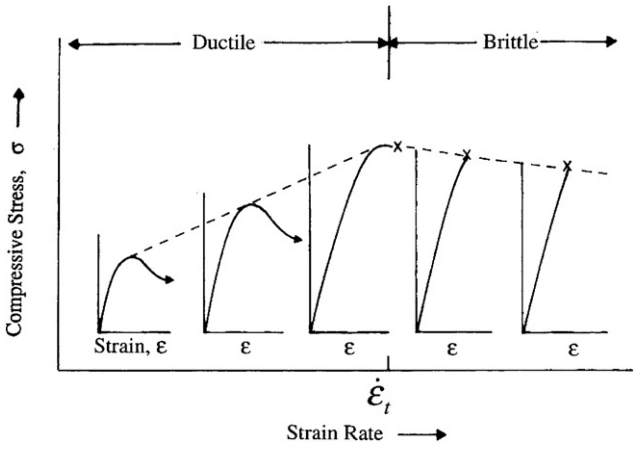

Fig. 1. Modes of failure in ice as a function of strain rate. Reprinted from Schulson (2001).

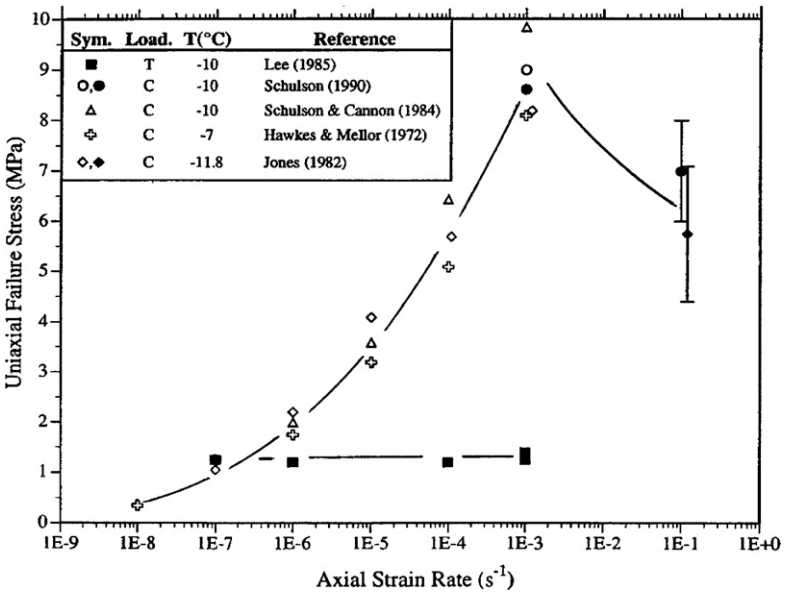

Fig. 2. Flow stress as a function of strain rate. Reprinted from Schulson (2001).

ductile to brittle transition occurs at a strain rate on the order of 10^{-3} s^{-1}, under uniaxial compression, at temperatures on the order of −10 °C. Schulson (2001) (see Fig. 2) shows a dramatic increase for polycrystal ice in the compressive failure stress from 0.5 MPa at a strain rate of 10^{-8} s^{-1} to 10 MPa at a strain rate of 10^{-3} s^{-1} then a decline to 6 MPa at 10^{-1} s^{-1} (with considerable scatter in the data).

Cole (2001) reported that in the range 10^{-2} s^{-1} to 10^{-1} s^{-1} the failure stress was independent of the rate. Dutta (1993) and Dutta et al. (2003) used a split Hopkinson bar to investigate the strain rate sensitivity of the compressive failure of polycrystalline ice for strain rates ranging from 10^{0} s^{-1} to 10^{2} s^{-1}. He reports that within that regime the compressive failure stress was rate independent.

In recent single crystal tests using thin samples in a Hopkinson bar, Shazly et al. (2005) observe an increase in compressive failure stress from 20 MPa at 90 s^{-1} to 34 MPa at 882 s^{-1}. A fit to their data, using a static compressive failure stress of 14.8 MPa for single crystal ice is shown in Fig. 3. Note that the static failure stress for the single crystal ice is twice the value given by Schulson for polycrystal ice. According to Schulson (2004),

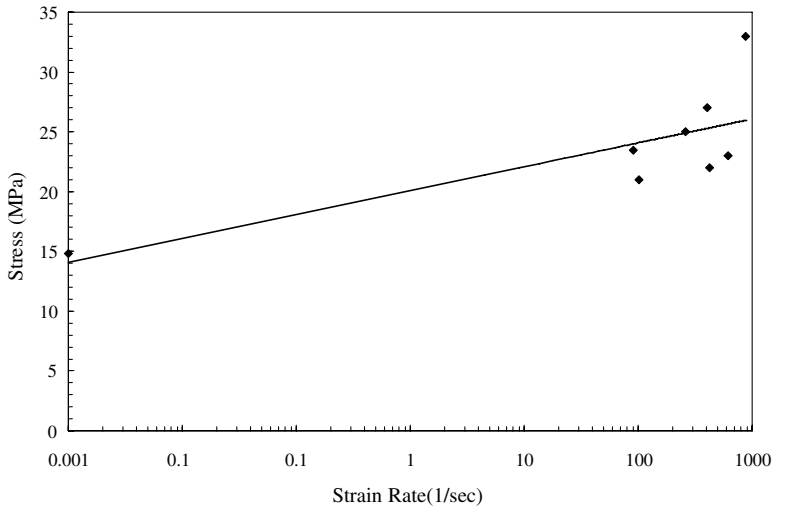

Fig. 3. Strain rate sensitivity for single crystal ice.

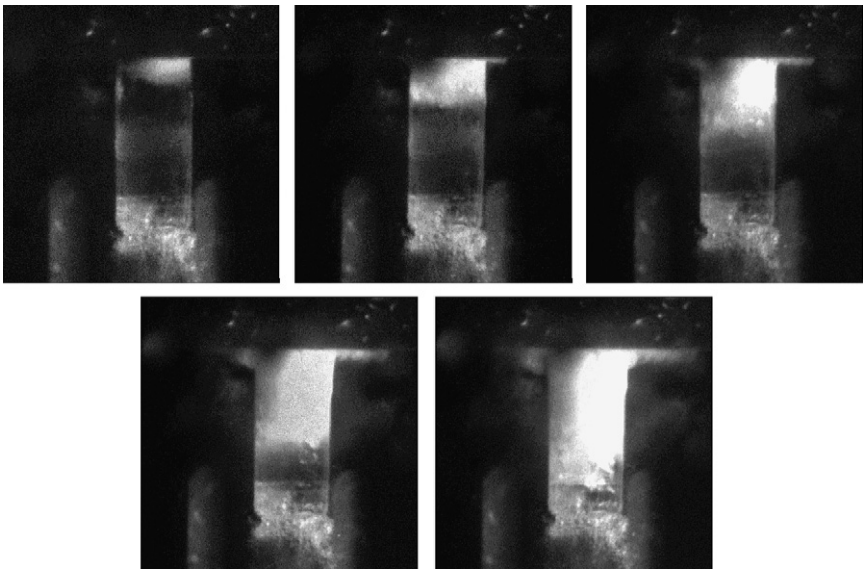

Fig. 4. Damage propagation at the speed of sound in ice. The damage is indicated by a loss of transparency in the ice.

at −10 °C the Ice Culture single crystal ice is one of the strongest ices he has tested. By using single crystal ice as test specimens, the normal scatter in the ice strength is minimized, allowing the strain rate sensitivity of ice to be observed.

To summarize the rate sensitivity tests, polycrystalline and single crystal ice is strain rate sensitive from 10^{-8} s^{-1} to 10^{-2} s^{-1}, while single crystal ice has now been shown to exhibit rate dependency from $\sim 10^{0}$ s^{-1} to 10^{3} s^{-1}. It is not known whether or not there are fundamentally different mechanisms limiting the strength in the polycrystalline and single crystal samples. This is a possibility given the grain size dependence of the static compressive failure stress.

Experiments (see Fig. 4 from Pereira et al. (2006)) indicate that the damage in ice, as gauged by its loss of transparency, can propagate at approximately the sound speed. The cylindrical ice projectile was 1.25 in. diameter and 3 in. long, and before impacting a steel plate, its velocity was 680 ft/s. These photographs were taken at a frame rate of 260,010 frames per second and the calculated velocity of the fracture wave was approximately $\sim 10^{4}$ ft/s. Schulson (1990) and Smith and Schulson (1993) report that high speed photography shows that cracks first form in virgin ice after an applied stress of twenty to thirty percent of the failure stress.

Ice, like rock, concrete, and ceramics, typically exhibits residual strength after damage. The mechanism is usually hypothesized to be intergranular friction due to a positive pressure. A simple model for this type of behavior is the Mohr-Coulomb criterion where the failure stress and/or the residual flow stress are assumed to be linear functions of the pressure,

$$|\boldsymbol{\sigma}| = \sigma_f(\boldsymbol{\sigma}, \boldsymbol{q}, \dot{\epsilon}) + \mu \max(P, 0) \tag{3}$$

where $|\boldsymbol{\sigma}|$ is some norm of the stress, $\boldsymbol{q}$ is a vector of internal state variable (e.g., the equivalent plastic strain), and μ is the coefficient of friction. Schulson (2001) reports that there is fair agreement between the ratio of confined to unconfined biaxial stress using this criterion for columnar grains of ice, referred to as S2, from −2.5 °C to −40 °C and that the triaxial failure stress can also be rationalized to within a factor of 2.

Experiments (Fortt and Schulson, 2004; Kennedy et al., 2000; Montagnat and Schulson, 2003) indicate that at −30 °C and −40 °C, the coefficient of friction increases, and then decreases with increasing velocity, varies with temperature, and is insensitive to the pressure and the grain size. The maximum velocity in the experiments was low (<1 m/s) as were the pressures, (<1 MPa). It is therefore an open question whether the velocity sensitivity of the coefficient of friction appearing in Eq. (3) has saturated in high velocity impact experiments.

Damaged ice has been observed to sustain strains of 10% in high strain rate experiments by Fasanella and Kellas (2006). Schulson (2001) reports that at low rates of deformation that ice is ductile with a softening

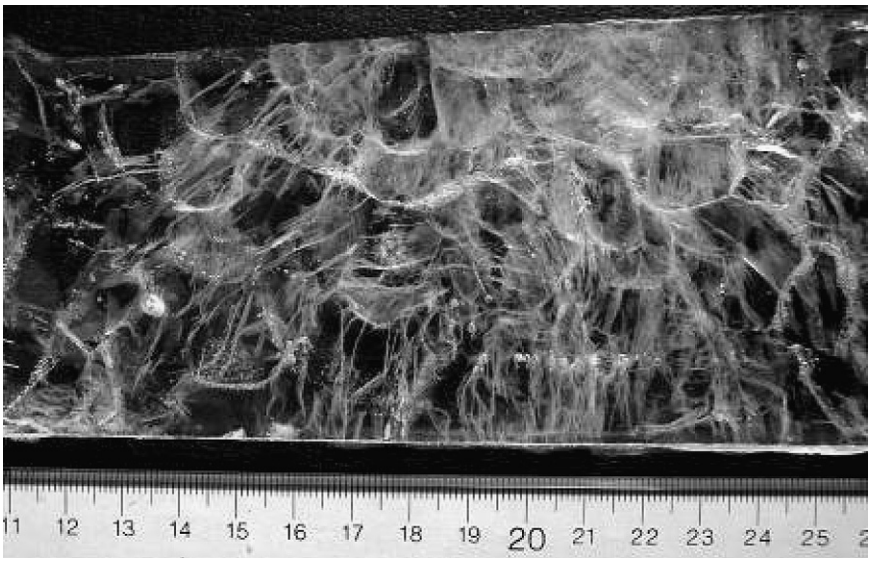

Fig. 5. Damaged ice under triaxial compression.

response after the peak stress, and that it can sustain plastic strains of up to 10% without macroscopic collapse in unconfined experiments although it is profusely cracked. Between the two regimes is a brittle response where the plastic strains are limited to a fraction of a percent. It is possible that at high strain rates, localized adiabatic heating at the crack faces may result in melting, increasing the cohesive strength in the damaged ice. To separate two surfaces ''bonded'' by a thin layer of water requires either a force sufficient to cavitate the water or sufficient time to allow the inflow of water from the boundaries, which would appear as a visco-elastic response. Another possible explanation for the apparently ductile behavior is a combination of high coefficients of friction within the ice and the complex cracked geometry of the ice. A photograph, from Schulson et al. (2005), of a typical cracked ice structure is shown in Fig. 5.

3. High velocity ice impact computational modeling background

The literature for modeling high velocity ice impacts is very small, which is not too surprising considering that only recently has the computational power become available for this type of simulation and the market for this research is a narrow segment of the aerospace industry.

Two papers (Kim and Kedward, 2000; Kim et al., 2003) modeling the impact of hail on composites were found. The computational results were compared to simulated hail ice fired from a nitrogen gas cannon. Their simulations were performed using a 1993 version of DYNA3D (Whirley and Engelmann, 1993), an explicit

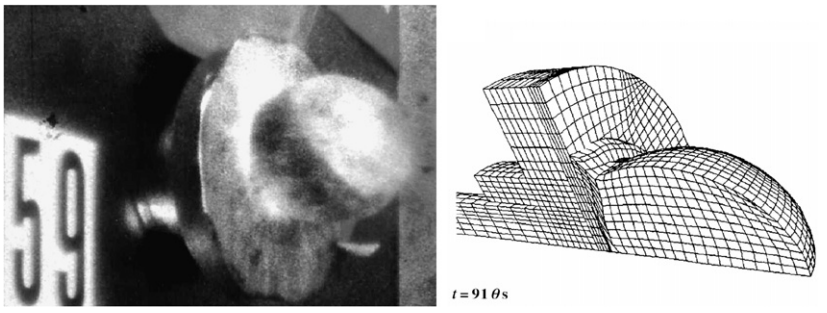

Fig. 6. Comparison of an experiment to a calculation of a 42.7 mm diameter ice ball fired at 73.5 m/s at a time of 91 μs. Reprinted from Kim and Kedward (2000).

Lagrangian finite element program originally developed at Lawrence Livermore National Laboratory by Hallquist (1976). Fig. 6 shows an image from an experiment and the calculated result for a 42.7 mm diameter ice ball fired at 73.5 m/s at a time of 91 μs, which corresponds to the time of the peak impact force. There is clearly a good agreement between test and experiment on the deformed shape of the projectile. The time histories of the calculated and measured impact force show good agreement as do the calculated and measured strain histories in the target. The authors report that the projectile fails locally and microcracking is evident throughout the projectile.

A simple isotropic elastic–plastic material model with failure was used in the calculations. To handle the large rotations, the Jaumann stress rate, $\overset{\mathrm{J}}{\boldsymbol{\sigma}}$,

$$\overset{\mathrm{J}}{\boldsymbol{\sigma}} = \dot{\boldsymbol{\sigma}} - \boldsymbol{\sigma}\boldsymbol{\omega} - \boldsymbol{\omega}\boldsymbol{\sigma} \tag{4}$$

$$\boldsymbol{\omega} = \frac{1}{2}(\boldsymbol{L} - \boldsymbol{L}^{\mathrm{T}}) \tag{5}$$

is used, where $\dot{\boldsymbol{\sigma}}$ is the material stress rate, $\boldsymbol{\omega}$ is the spin, and $\boldsymbol{L}$ is the velocity gradient. The stress is expressed in terms of its deviatoric component and the pressure,

$$\boldsymbol{\sigma} = \boldsymbol{\sigma}' - P\boldsymbol{I}. \tag{6}$$

Using standard J_2 flow theory, the deviatoric stress rate is

$$\overset{\mathrm{J}}{\boldsymbol{\sigma}'} = 2G(\boldsymbol{D} - \boldsymbol{D}^{\mathrm{p}}) \tag{7}$$

$$\boldsymbol{D}' = \boldsymbol{D} - \frac{1}{3}\mathrm{tr}(\boldsymbol{D})\boldsymbol{I} \tag{8}$$

where G is the shear modulus, $\boldsymbol{D}$ is the deformation rate, and $\boldsymbol{D}^{\mathrm{p}}$ is the plastic strain rate. The equivalent stress, $\bar{\sigma}$ for J_2 flow theory is

$$\bar{\sigma} = \sqrt{\frac{3}{2}\boldsymbol{\sigma}' : \boldsymbol{\sigma}'}. \tag{9}$$

The plastic strain rate enforces the yield stress constraint

$$\bar{\sigma} = \sigma_{\mathrm{Y}} + h\bar{\epsilon}^{\mathrm{p}} \tag{10}$$

$$\bar{\epsilon}^{\mathrm{p}} = \int_0^t \sqrt{\frac{2}{3}\boldsymbol{D}^{\mathrm{p}} : \boldsymbol{D}^{\mathrm{p}}}\,\mathrm{d}t \tag{11}$$

where σ_{Y} is the initial yield stress and h is the hardening parameter.

The pressure in the ice is

$$P = K\left(\frac{\rho}{\rho_0} - 1\right) \tag{12}$$

where K is the bulk modulus, ρ is the density, and ρ_0 is the initial density.

The failure model sets the deviatoric stress to zero and limits the pressure to be positive after

$$\bar{\epsilon}^{\mathrm{p}} > \bar{\epsilon}^{\mathrm{p}}_{\mathrm{fail}} \quad \text{or} \quad P < P_{\mathrm{fail}} \tag{13}$$

where $\bar{\epsilon}^{\mathrm{p}}_{\mathrm{fail}}$ and P_{fail} are material parameters.

In terms of the engineering properties discussed in the previous section, the limitations of the model are:

(1) The yield stress is not a function of the strain rate or pressure.
(2) The plastic hardening modulus, h, of the material was tuned arbitrarily to match the ballistic test data.
(3) The failure stress, $\sigma_{\mathrm{Y}} + h\bar{\epsilon}^{\mathrm{p}}_{\mathrm{fail}}$, is the same for both tension and compression, and is not a function of the strain rate or pressure.

A number of factors account for the success of this simple model in modeling the hail impact. First, the moderate impact velocities only produce moderate strain rates. Second, Hertzian contact between the

spherical projectile and the flat target result in the maximum stress, where the failure occurs, always being compressive. Since most of the projectile remains intact, the failure model has less of a role than in a problem where the projectile completely fragments. Finally, the properties of this ice material model were tuned to the response of their particular test. When this model was implemented for use in ballistic impact at velocities of interest to our program, using a cylinder instead of a sphere, the ice in the simulation did not fragment. As a result, the calculated force in the load cell model did not match the measured test data.

4. A rate sensitive plasticity model for ice with failure

Safety calculations are naturally conservative; the ice model presented here was developed to model a strong ice with repeatable properties. In particular, the ice examined here is a single crystal, optically clear ice free of initial cracks. The model presented here does not include a temperature dependency despite ice being a temperature dependent material. Given that the duration of an impact experiment is measured in milliseconds, the temperature of the ice is assumed constant during the simulation. The temperature of the ice that forms on the Shuttle varies with its distance from the cold source, and is almost impossible to measure in situ. The temperature of -10 °C is a common value at which the strength of ice is reported. In addition, at -10 °C ice exhibits brittle behavior over the range of strain rates of interest. Therefore, all experiments are performed at this temperature and all data used in the model are also evaluated at this temperature or are largely temperature independent. Although this model was developed for very strong ice, we have also used it for weaker, more commonly encountered ice types with the appropriate compressive strength selected.

This model uses tabular data, and interpolation between the specified points, in preference to analytical functions for defining the dependence of the flow stress on the strain rate and pressure. The direct use of tabular data eliminates the time consuming intermediate step of fitting the experimental data to the analytical relations, and eliminates the error between the measured response and the analytical relations. To emphasize which functions are tabular, a caret ($\hat{\cdot}$) is placed over them.

The flow stress has a product form,

$$\bar{\sigma} = \hat{s}(|\boldsymbol{D}|, P) \cdot \hat{\sigma}_f(\bar{\epsilon}^{\mathrm{p}}) \tag{14}$$

The scaling function, $\hat{s}$, is composed of two tabular functions of the strain rate at a specified pressure, and the scaling function is determined by interpolating between them based on the pressure

$$\hat{s}(|\boldsymbol{D}|, P) = f \cdot \hat{c}_{\mathrm{C}}(|\boldsymbol{D}|) + (1 - f) \cdot \hat{c}_{\mathrm{T}}(|\boldsymbol{D}|) \tag{15}$$

$$f = \min\left(1, \max\left(0, \frac{P - P_{\mathrm{T}}}{P_{\mathrm{C}} - P_{\mathrm{T}}}\right)\right) \tag{16}$$

The subscripts C and T indicate compression and tension, respectively, and $\hat{c}_{\mathrm{C}}$ and $\hat{c}_{\mathrm{T}}$ are tabular functions of the strain rate at the constant pressure P_{C} and P_{T}, respectively. Note that there is no extrapolation of the data. If the material has failed, the pressure used to evaluate the flow stress is $\max(0, P)$.

Two different norms for the strain rate have been evaluated. The first is based on the deviatoric part of the deformation rate,

$$|\boldsymbol{D}| = \sqrt{\frac{2}{3}\boldsymbol{D}' : \boldsymbol{D}'} \tag{17}$$

The second is simply the Euclidian norm of $\boldsymbol{D}$,

$$|\boldsymbol{D}| = \sqrt{\boldsymbol{D} : \boldsymbol{D}}. \tag{18}$$

In the calculations presented here, we use Eq. (17).

The pressure is evaluated using a tabulated equation of state with compaction,

$$P_{\mathrm{EOS}} = \widehat{C}(\epsilon_V) + \gamma \widehat{T}(\epsilon_V) E \tag{19}$$

$$\epsilon_V = \ln(V/V_0) \tag{20}$$

where V_0 is the reference specific volume, E is the internal energy per reference volume, $\widehat{C}$ and $\widehat{T}$ are tabular functions, and γ is the Gruneisen coefficient. In our calculations, γ is zero. Unloading occurs linearly with the

bulk modulus at the peak volume strain, and reloading occurs along the same line. A pressure cut-off limits the magnitude of the pressure in tension,

$$P = \max(P_{\text{EOS}}, P_{\text{cut-off}}). \tag{21}$$

where $P_{\text{cut-off}} = \hat{s}P^0_{\text{cut-off}}$ and the parameter $P^0_{\text{cut-off}}$ is the static pressure cut-off, which are evaluated separately in both tension (P_{T}) and compression (P_{C}). After the material fails, $P_{\text{cut-off}}$ is set to zero. While $\hat{s}$ is formally a function of the current pressure P, it is evaluated using P_{EOS}.

Although the pressures in the ice are below the shock pressures where a nonlinear response would be expected and ice/water is volumetrically elastic, the compaction feature of the equation of state has facilitated the matching of the calculated response to the experiment. In the analysis using the linearly elastic equation of state (Eq. (12)), unrealistic pressure oscillations occurred in the damaged ice. These pressure waves are not observed in the ballistic tests. These oscillations are minimized in the ice model by use of the compaction feature of the equation of state. No direct, applicable test data was available and so this relation was derived heuristically. A graph of $P - \epsilon_V$ is shown in Fig. 7.

We have implemented two failure models. The final stress is

$$\boldsymbol{\sigma} = d^e \cdot d^P \cdot (\boldsymbol{\sigma}' - P\boldsymbol{I}). \tag{22}$$

where d^e and d^P are the damage variables associated with the failure due to plastic strain and pressure respectively. The failure criterion for plastic strain is

$$d^e = \begin{cases} 0 & \text{if } \bar{\epsilon}^{\text{p}} > \bar{\epsilon}^{\text{p}}_{\text{fail}} \\ 1 & \text{otherwise} \end{cases} \tag{23}$$

and for pressure it is

$$d^P = \begin{cases} 0 & \text{if } P > P_{\text{cut-off}} \quad \text{or} \quad P < P^{\text{T}}_{\text{fail}} \\ 1 & \text{otherwise} \end{cases} \tag{24}$$

The values for the pressure cut-off terms and other ice model parameters are included in Table 2. These are typical for ice. In addition, the compressive strain rate behavior, plotted in Fig. 3, is included in tabular form as shown in Table 3. These parameters, which can be obtained by direct material testing, are the only inputs required by the ice model. The tensile strain behavior was unavailable and so the tensile strain rate sensitivity was assumed to be constant. The plasticity function, $\hat{\sigma}_f$ was assumed to have linear hardening with different initial values in compression and tension due to limited data.

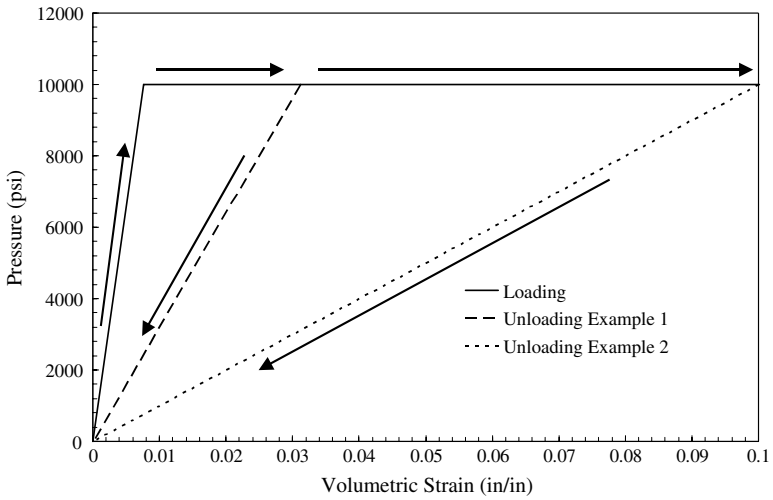

Fig. 7. Equation of state with loading and unloading.

Table 2
Ice model input parameters for strong ice at −10 °C

ρ	Density	897.6 kg/m^3
E	Young's modulus	9.31 GPa
$\hat{\sigma}_f^{\mathrm{C}}$	Initial compressive flow stress	172.4 MPa
$\hat{\sigma}_f^{\mathrm{T}}$	Initial tensile flow stress	17.24 MPa
h	Plastic tangent modulus	6.89 MPa
v	Poisson's ratio	0.33
P_{C}	Pressure cut-off in compression (dependent on ice structure)	Single crystal: 4.93 MPa polycrystal: 3.0 MPa
P_{T}	Pressure cut-off in tension	0.433 MPa

Table 3
Strain sensitivity of ice

Strain rate, s^{-1}	Stress scale factor
1.0	1.00000
10.0	1.25660
100.0	1.51320
200.0	1.59044
300.0	1.63562
400.0	1.66768
500.0	1.69255
600.0	1.71287
700.0	1.73005
800.0	1.74493
900.0	1.75805
1000.0	1.76979
1100.0	1.78042
1500.0	1.81498
10000.0	2.02639

Two additional features have been implemented in the model but have not been used in the safety calculations due to the absence of sufficient data to calibrate them. Nevertheless, we believe that they will improve the accuracy of the calculations once the appropriate values have been determined.

The first allows the failed ice to retain some small amount of residual strength after the ice has failed according to d^e and d^P,

$$\bar{\boldsymbol{\sigma}} = \begin{cases} \delta \cdot \hat{s}(|\boldsymbol{D}|, \bar{\epsilon}^{\mathrm{p}})\hat{\sigma}(\bar{\epsilon}^{\mathrm{p}}) & \text{if } d^e \cdot d^P = 0 \\ \hat{s}(|\boldsymbol{D}|, \bar{\epsilon}^{\mathrm{p}})\hat{\sigma}(\bar{\epsilon}^{\mathrm{p}}) & \text{otherwise} \end{cases} \tag{25}$$

$$\boldsymbol{\sigma} = \boldsymbol{\sigma}' - P\boldsymbol{I} \tag{26}$$

where δ is a small number. This retention of residual strength has been observed in testing (Shazly et al., 2005; Fasanella and Kellas, 2006), but quantitative data has not been obtained. The pressure cut-off is still set to zero if $d^e \cdot d^P = 0$.

The second addition is a visco-elastic term, $\boldsymbol{\sigma}'_{\mathrm{v}}$, that is added to the stress,

$$\boldsymbol{\sigma} = \boldsymbol{\sigma}' + \boldsymbol{\sigma}'_{\mathrm{v}} - P\boldsymbol{I} \tag{27}$$

where the visco-elastic stress is calculated using a Prony series,

$$\boldsymbol{\sigma}'_{\mathrm{v}} = \int_0^t g(t-\tau)\frac{\partial \boldsymbol{D}'}{\partial \tau}\,\mathrm{d}\tau \tag{28}$$

$$g(t) = \sum_{i=1}^{N} G_i \mathrm{e}^{-\beta_i t} \tag{29}$$

5. Calculations and comparison to experiments

5.1. Finite element formulation

The material model was implemented in LS-DYNA (Hallquist, 1998)[1] and the calculations were performed using the explicit, multi-material Eulerian formulation for the projectile and a Lagrangian formulation for the target. The Eulerian projectile interacts with the Lagrangian finite element model of the target through a penalty contact formulation. LS-DYNA is a commercial finite element program that started with a public domain version of the DYNA3D program used by Kim and Kedward (2000) and Kim et al. (2003). In contrast to earlier simulation efforts, the entire projectile fragments, leading to a nearly liquid behavior at late times, see Fig. 8. A Lagrangian formulation for the projectile fails at late times because of the extreme mesh distortion and tangling.

Since the multi-material Eulerian formulation is less commonly used than the Lagrangian formulation in solid mechanics, a brief summary of the formulation is presented; more detail about the numerical algorithms is presented in Benson (1992). Most multi-material Eulerian formulations rely on the operator splitting (Chorin et al., 1978) of the Eulerian equations,

$$\frac{\partial \rho}{\partial t} + \nabla \cdot (\rho \boldsymbol{u}) = 0 \tag{30}$$

$$\frac{\partial \rho \boldsymbol{u}}{\partial t} + \nabla \cdot (\rho \boldsymbol{u} \otimes \boldsymbol{u}) = \nabla \cdot \boldsymbol{\sigma} + \rho \boldsymbol{b} \tag{31}$$

$$\frac{\partial \rho e}{\partial t} + \nabla \cdot (\rho e \boldsymbol{u}) = \boldsymbol{\sigma} : \boldsymbol{D} \tag{32}$$

where ρ is the density, $\boldsymbol{u}$ is the velocity, $\boldsymbol{x}$ is the spatial coordinate, and e is the internal energy per current volume.

The equations have the same form as the model conservation equation for a variable ϕ with a source term Φ,

$$\frac{\partial \phi}{\partial t} + \nabla \cdot (\phi \boldsymbol{u}) = \Phi. \tag{33}$$

This equation may be solved sequentially by first solving the "Lagrangian" equation

$$\frac{\partial \phi}{\partial t} = \Phi \tag{34}$$

then the "Eulerian" equation, which is associated with the transport of material between elements,

$$\frac{\partial \phi}{\partial t} + \nabla \cdot (\phi \boldsymbol{u}) = 0. \tag{35}$$

The Lagrangian step for the Eulerian formulation is nearly identical to the time step performed by a standard explicit finite element formulation. During this step, both the Lagrangian and Eulerian meshes behave in a Lagrangian manner, and they are coupled using a penalty formulation (Benson, 1992).

The transport during the Eulerian step is often viewed (and implemented) as an incremental projection or "rezone". The similarities between material transport algorithms and rezoning are well known (Johnson, 1992; Dukowicz, 1984). Second order accurate methods (Benson, 1992) are used to provide an accurate, stable solution.

5.2. Ballistic impact tests and setup

In order to validate the analytical ice model, a short series of impact tests on an instrumented fixture, inside of a vacuum chamber, were conducted by Pereira et al. (2006). A compressed helium gas gun was used to

[1] At the request of NASA, this model is available in the production version of LS-DYNA as material model 155 with the keyword input *MAT_PLASTICITY_COMPRESSION_TENSION_EOS.

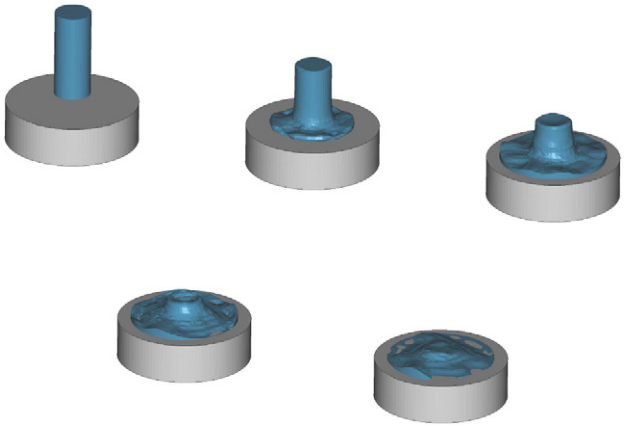

Fig. 8. Solid to fluid transition using an Eulerian formulation.

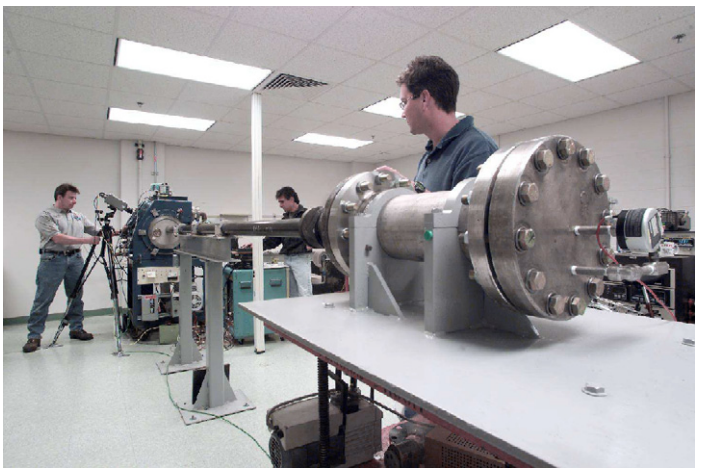

Fig. 9. Two inch vacuum gun.

accelerate a sabot which carried an ice projectile. This gun is pictured in Fig. 9. A sabot catcher at the end of barrel caught the sabot and held back the gases from the gun, maintaining the vacuum in the test chamber. Using the vacuum chamber contributes to a more controlled impact and cleaner data. Cylindrical ice projectiles, both single crystalline and polycrystalline, of 0.6875 in. diameter and 1.66 in. length, were targeted on a circular steel plate of 2.5 in. diameter and 0.75 in. thickness. Gun pressure was varied such that the ice projectiles were traveling at approximately 300, 500 and 700 ft/s when they impacted the instrumented plate. The input parameters for the ice model are given in Tables 2–4.

Tests were conducted with the plate normal to the trajectory vector, and at a 45° angle to the trajectory vector. Immediately behind the plate was a single pre-loaded, washer type PCB 260A13 load cell. The data

Table 4
Equation of State loading table

ln Volumetric strain	Pressure (psi)	Bulk modulus (psi)
0.0	0	1.3×10^6
-7.693×10^{-3}	10^4	1.3×10^6
-3.125×10^{-2}	10^4	3.2×10^5
-10	10^4	1.0×10^3

was processed using a 25 kHZ anti-aliasing filter. Running through the load cell was a bolt, by which the target plate was attached to the appropriate backup structure. A photograph of the normal test configuration is shown in Fig. 10.

The steel target plate was rigid in the frequency range of interest, but the load cell, bolt, and backup structure assembly was not. A modal survey was conducted of both the normal test configuration and the 45° test configuration. A photograph of the 45° test configuration during the modal survey is shown in Fig. 11.

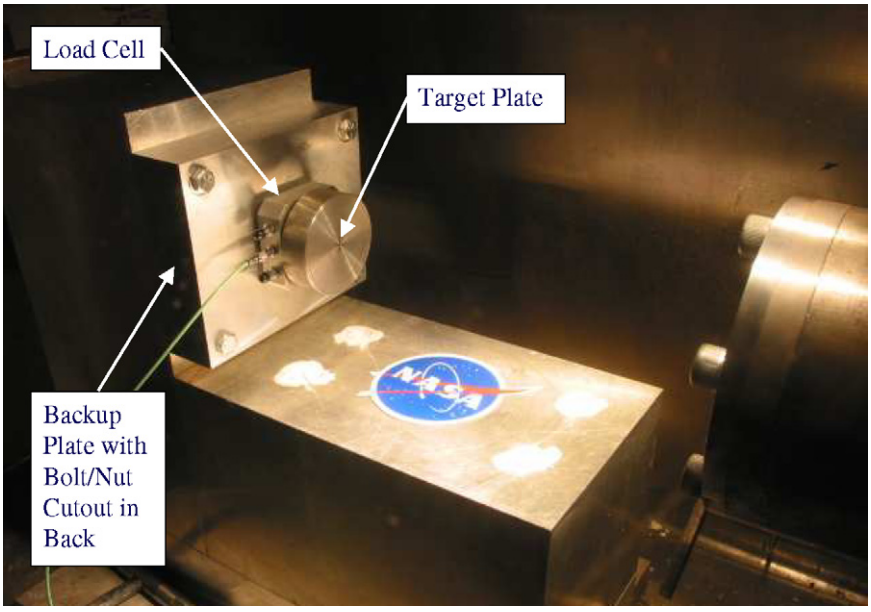

Fig. 10. Target plate in the normal configuration.

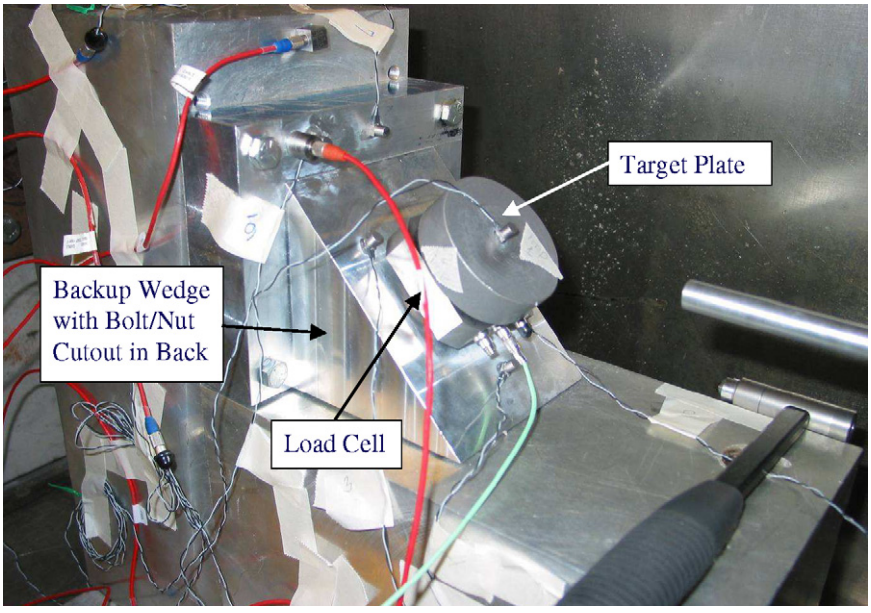

Fig. 11. Target plate in the 45° configuration with modal survey instrumentation.

The design of the target plate was a compromise between rigidity for load transfer, and low mass for contact force transmissibility. While the plate is sufficiently rigid, its inertia is large enough for the contact force to be somewhat attenuated before it reaches the load cell.

5.3. Comparison of calculated and experimental results

In order to accurately compare test and analysis, the finite element model of the test included the target plate, and simple representations of the load cell, the bolt, and the backup structures, which were correlated with the results of the modal survey,as shown in Fig. 12. The force time history of the analytical representation of the load cell was filtered at 25 kHZ, similar to the filtering of the test data, and compared to the test data. As can be seen in Figs. 13 (300 ft/s), 14 (500 ft/s), and 15 (700 ft/s), the match between analysis and test is

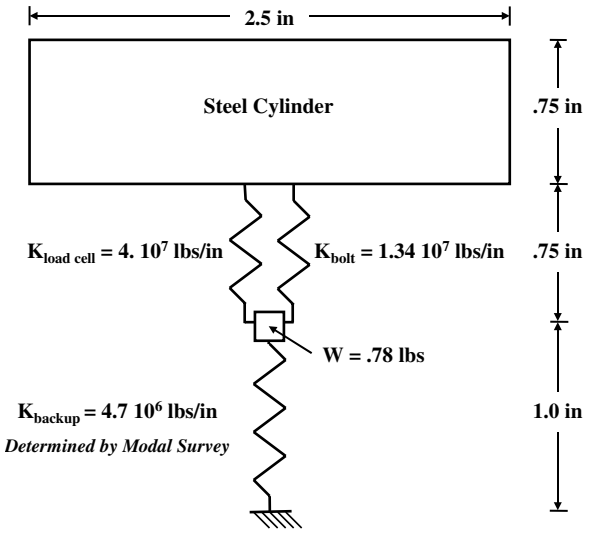

Fig. 12. Analysis representation of test setup.

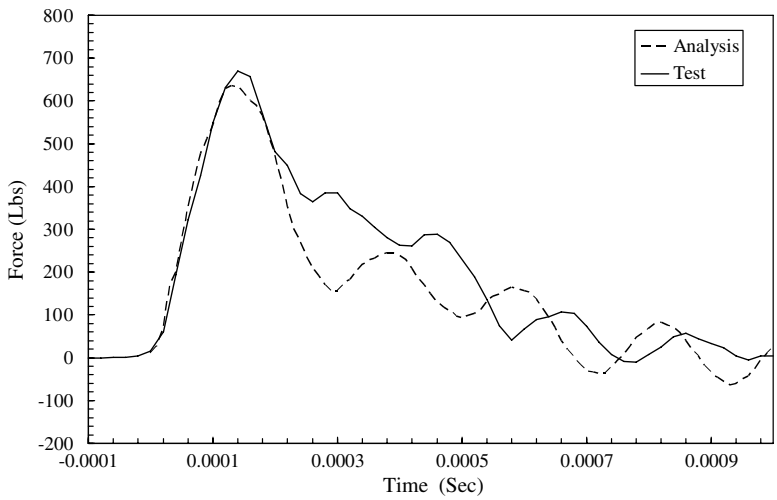

Fig. 13. Test analysis comparison at 300 ft/s, normal orientation.

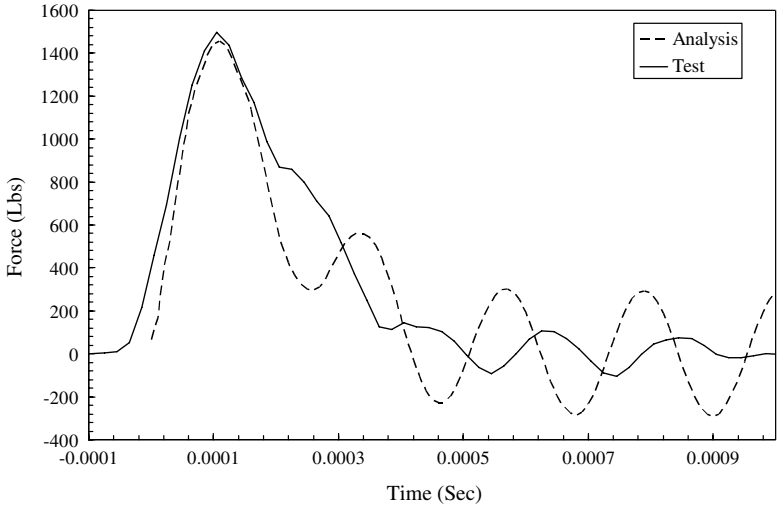

Fig. 14. Test analysis comparison at 500 ft/s, normal orientation.

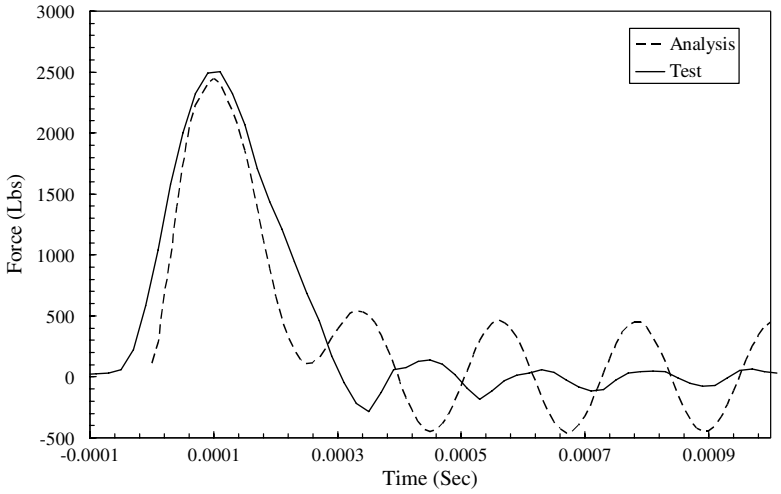

Fig. 15. Test analysis comparison at 700 ft/s, normal orientation.

good. The absence of damping in the analysis explains the ringing in the computed response compared to the relatively smooth decay of the test signal in the experiment.

To a certain extent, matching the test with the analysis is made somewhat easier by the attenuation due to the inertia of the target plate. The actual contact force partially consists of a very short duration impulse which is difficult to capture in the ballistic test laboratory. Additional testing will be performed in an alternate test setup to try to capture this impulse. A plot of the calculated contact force is shown in Fig. 16.

Comparisons of test and analysis for the 45° configuration were also made. Again, the comparison is good and is shown in Figs. 17 and 18.

Additional comparisons were made at much lower velocities in the drop tower at NASA Langely Research Center (LaRC) (Fasanella and Kellas, 2006). Figs. 19 and 20 shows the comparison between the test data and the analytical predictions. The shape of the ice used in the slower velocity drop (20.4 ft/s), was a cylinder with a half sphere on its contact side. In the higher velocity drop (100 ft/s), the shape of the ice was a simple

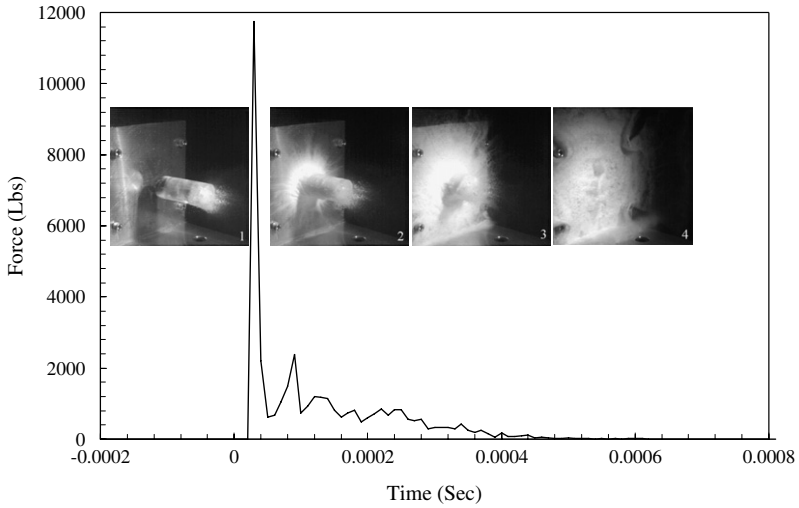

Fig. 16. Computed contact force at 500 ft/s.

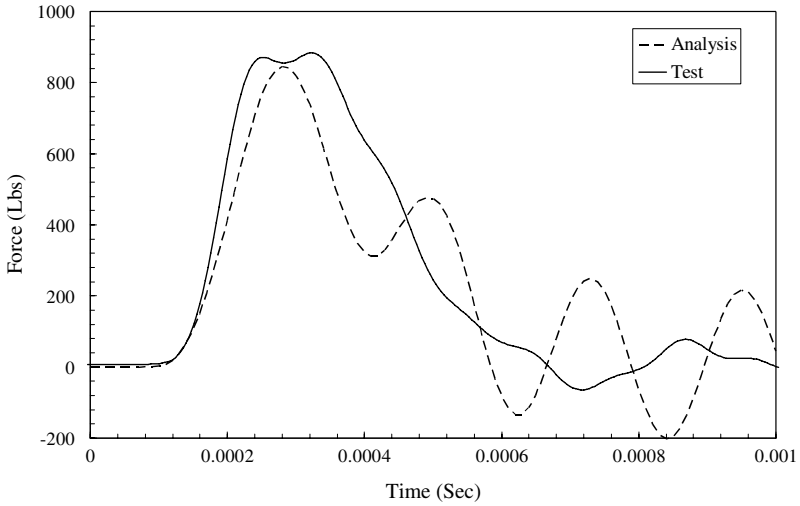

Fig. 17. Test analysis comparison at 500 ft/s, 45° setup.

cylinder and so its contact surface was flat. The varying ice geometry, in addition to the significant difference in velocity, explains the qualitative difference in the data between the two tests. The analysis using the ice model was successful in predicting the differing qualitative responses.

It should be noted that at the lowest initial velocities, there was a significant test to test variance in the measured LaRC drop tower forces. At the lowest initial velocities the static properties of the ice, such as shown in Table 1, govern the forced response. Therefore, the large variances in the static properties of the ice are reflected in the force response variance. As velocities increase the initial kinetic energy of the ice projectile gains in importance, thereby leading to increased repeatability of force response test data.

Some of the experiments described in Kim and Kedward (2000) and Kim et al. (2003) were also modeled using the ice model. A comparison of Kim and Kedward Test 54, a 1.68 in. diameter ice sphere impacting at an initial velocity of 413 ft/s, is shown in Fig. 21. The ice compressive strength for this calculation was estimated using the specified ice structure as 5.15 MPa.

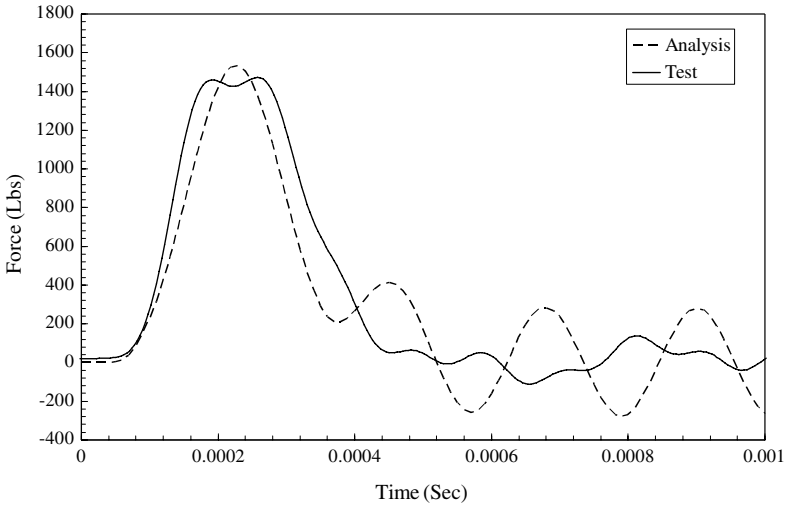

Fig. 18. Test analysis comparison at 700 ft/s, 45° setup.

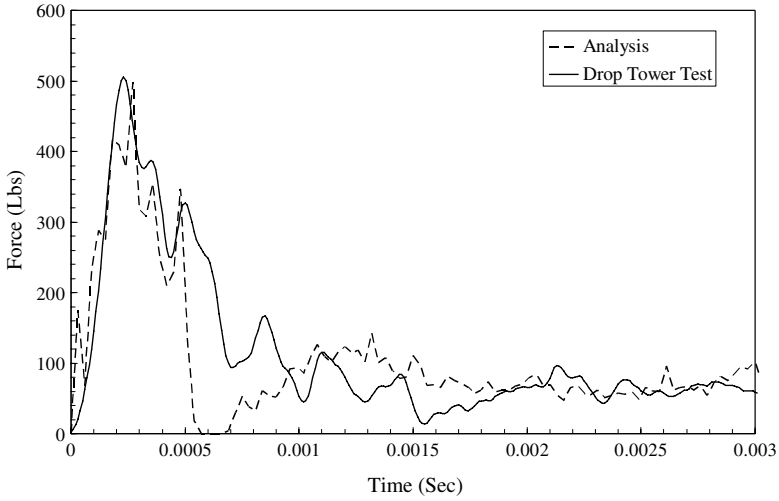

Fig. 19. Test analysis comparison from the LaRC drop tower at 20.4 ft/s.

6. Discussion

The physical phenomena which are important to capture, and are included in this ice model, are:

(1) The separate failure stresses when the ice is in tension or compression. This is a well known property of ice (Schulson, 2001). While the ballistic test results, which are dominated by compressive failure, are probably not sensitive to this feature, other configurations of ice impact can be.
(2) Compressive failure is a function of the strain rate. The importance of this feature is amply demonstrated by the test results at varying velocities.
(3) Once failure has occurred, the ice's ability to carry deviatoric stress is sharply curtailed, or eliminated. Omitting this feature produces unrealistically high peak stresses in calculations that are not shown.
(4) Once the deviatoric stresses have been scaled, or eliminated, the ice flows like a fluid, and this can only be modeled using an Eulerian formulation or periodic rezoning.

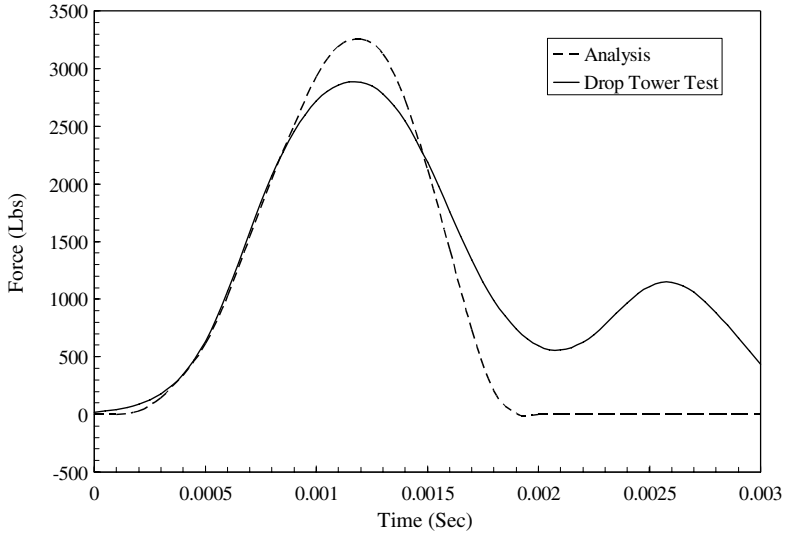

Fig. 20. Test analysis comparison from the LaRC drop tower at 100 ft/s.

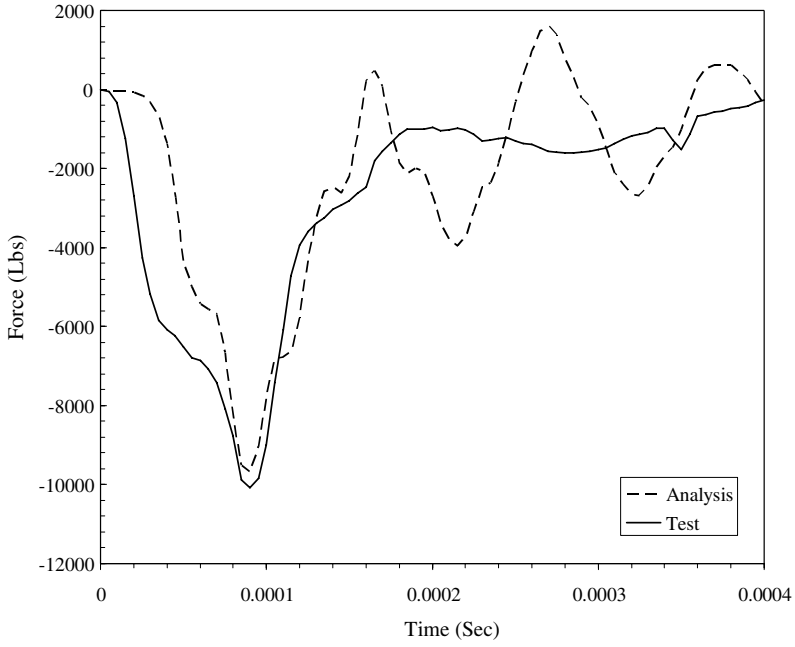

Fig. 21. Test analysis comparison of Kim and Kedward Test 54; 1.68 in. diameter sphere at 413 ft/s.

(5) Once failure has occurred, the ability of the ice to carry hydrostatic stress is not altered, allowing it to maintain load on the impact target. Omitting this feature and the deviatoric stress after failure would results in the ice exerting zero stress.
(6) The tabulated equation of state with compaction has been utilized to reduce physically unrealistic stress waves in ice which has failed, but has not yet impacted the target.

Based on the less extensive testing of this model for weaker ice, the model appears to be reasonably accurate if the compressive strength of the ice is set to the static compressive failure value for that particular ice

structure. Weaker ice tends to have less consistent properties than the strong, single crystal ice used in the model development. As a result matching impact experiments with any deterministic ice model becomes more difficult, particularly at lower velocities where the structural properties of the ice dominate.

7. Summary and conclusions

A phenomenological model for ice has been developed and its predicted results compared to experiments. The agreement between the two is both quantitatively and qualitatively better than with other ice models we have tried. Based on the experience gained during the development of this model, the critical aspects of its success are the independent failure stress in tension and compression, the strain rate sensitivity of the flow stress, the ability of the failed ice to continue to carry hydrostatic stress and the use of the Eulerian mesh.

The model has been shown to work for multiple conditions and test setups. The input to the model is primarily based on clearly defined mechanical property tests, and requires no adjustments based on ballistic test data. For other than single crystal ice, the model appears to be reasonably accurate, if the material parameters are selected accordingly.

Experiments have shown that the phenomenology of ice at high strain rates has some qualitative similarities to other brittle materials, however modeling it with classical ceramic models has not produced accurate results. Additional experimental work is necessary for building the data base needed to develop a better model of ice based on physically motivated failure mechanisms.

Acknowledgements

The authors would like to thank the following people who significantly contributed to this effort; for providing test data and insight into ice, Erland Schulson (Dartmouth), Mike Pereira, Santo Padula, Duane Revilock, Jeff Hamel, Brad Lerch, Matt Melis (Glenn Research Center), Vikas Prakash, Mostafa Shazly (Case Western Reserve University), Ed Fasanella, and Sotiris Kellas (Langley Research Center), and for providing assistance in the analysis, Mike Bennett (U of Akron) and John Hallquist (LSTC).

References

Benson, D.J., 1992. Computational methods in Lagrangian and Eulerian hydrocodes. Computer Methods in Applied Mechanics and Engineering 99, 235–394.

Columbia Accident Investigation Board, 2003. Columbia accident investigation report. Tech. Rep., NASA.

Carter, D., 1971. Lois et mechanisms de l'apparente fracture fagile de la glace de riviere et du rac. Ph.D. thesis, de L'universite Laval.

Chorin, A., Hughes, T.J.R., McCracken, M.F., Marsden, J.E., 1978. Product formulas and numerical algorithm. Communication of Pure and Applied Mathematics 31, 205–256.

Cole, D.M., 2001. The microstructure of ice and its influence on mechanical properties. Engineering Fracture Mechanics 68 (17–18), 1797–1822.

DeWolfe, P.H., 1983. Ice impact testing of space shuttle thermal protection system materials. The Shock and Vibration Bulletin 53, 177–182.

Dukowicz, J.K., 1984. Conservative rezoning (remapping) for general quadrilateral meshes. Journal of Computational Physics 54, 411–424.

Dutta, P.K., 1993. Compressive failure of polycrystalline ice under impact. In: Proceedings of the Third (1993) International Offshore and Polar Engineering Conference, Singapore, pp. 573–580.

Dutta, P.K., Cole, D.M., Schulson, E.M., Sodhi, D.S., 2003. A fracture study of ice under high strain rate loading. In: Proceedings of the Thirteenth (2003) International Offshore and Polar Engineering Conference, Honolulu, Hawaii, pp. 465–472.

Fasanella, E., Kellas, S., 2006. Dynamic crush characterization of ice. Tech. Rep., NASA TM-2006-214278.

Fortt, A., Schulson, E.M., 2004. Post-terminal compressive deformation of ice: Friction along coulombic shear faults. In: Proceedings of the 17th International Symposium on Ice, St. Petersburg, Russia, pp. 315–322.

Hallquist, J.O., 1976. Preliminary user's manuals for DYNA3D and DYNAP (nonlinear dynamic analysis of solids in three dimensions). Tech. Rep. UCRL-52066, Lawrence Livermore National Laboratory.

Hallquist, J.O., 1998. LS-DYNA theoretical manual. Tech. Rep., Livermore Software Technology Corporation.

Johnson, C., 1992. A new approach to algorithms for convection problems which are based on exact transport + projection. Computer Methods in Applied Mechanics and Engineering.

Kennedy, F.E., Schulson, E.M., Jones, D.E., 2000. The friction of ice on ice at low sliding velocities. Philosophical Magazine A 80 (5), 1093–1110.

Kim, H., Kedward, K.T., 2000. Modeling hail ice impacts and predicting impact damage initiation in composite structures. AIAA Journal 38 (7), 1278–1288.

Kim, H., Welch, D.A., Kedward, K.T., 2003. Experimental investigation of high velocity ice impacts on woven carbon/epoxy composite panels. Composites Part A: Applied Science and Manufacturing 34, 25–41.

Montagnat, M., Schulson, E.M., 2003. On friction and surface cracking during sliding of ice on ice. Journal of Glaciology 49 (166), 391–396.

Pereira, J., II, S.P., Revilock, D., Melis, M., 2006. Force measurements in ballistic impact tests with ice projectiles. Tech. Rep., NASA TM-2006-214263.

Petrovic, J.J., 2003. Review mechanical properties of ice and snow. Journal of Materials Science 38, 1–6.

Schulson, E.M., 1990. The brittle compressive fracture of ice. Acta Metallurgica et Materialia 38 (10), 1963–1976.

Schulson, E.M., 2001. Brittle failure of ice. Engineering Fracture Mechanics 68, 1839–1887.

Schulson, E.M., 2004. Personal communication with K. Carney.

Schulson, E.M., Iliescu, D., Fortt, A., 2005. Characterizations of ice for return-to-flight of the space shuttle, part 1-hard ice. Tech. Rep., NASA CR-2005-213643-Part1.

Shazly, M., Prakash, V., Lerch, B., 2005. High strain rate compression testing of ice. Tech. Rep., NASA TM-2005-213966.

Smith, T.R., Schulson, E.M., 1993. The brittle compressive failure of fresh-water columnar ice under biaxial loading. Acta Metallurgica et Materialia 41 (1), 153–163.

Whirley, R.G., Engelmann, B.E., 1993. DYNA3D: A nonlinear, explicit, three-dimensional finite element code for solid and structural mechanics – user manual. Tech. Rep. UCRL-MA-107254, Rev. 1, Lawrence Livermore National Laboratory.